A Driving and Control Scheme of High Power Piezoelectric Systems over a Wide Operating Range

Tianyue Yang [1], Yuanfei Zhu [1] , Zhiwei Fang [1], Haoyu Wu [1], Wanlu Jiang [2] and Ming Yang [1],*

[1] Department of Instrument Science and Engineering, Shanghai Jiao Tong University, Shanghai 200240, China; thomas-yang@sjtu.edu.cn (T.Y.); zhuyuanfei@sjtu.edu.cn (Y.Z.); sjtufzw@sjtu.edu.cn (Z.F.); wuhaoyu@alumni.sjtu.edu.cn (H.W.)

[2] School of Mechanical Engineering, Yanshan University, Qinhuangdao 066000, China; wljiang@ysu.edu.cn

* Correspondence: myang@sjtu.edu.cn

Abstract: Significant variation in impedance under a wide range of loads increases the difficulty of frequency tracking and vibration control in high-power piezoelectric systems (HPPSs). This paper proposed a wide operating range driving and control scheme for HPPSs. We systematically analyzed the impedance characteristics and deduced the load optimization frequency. In order to provide sufficient drive capability, the inverter combined with an LC matching circuit is configured. With the aid of a transformer ratio arm bridge (TRAB) combined with a proposed pulse-based phase detector (PBPD), the proposed scheme can control the vibration amplitude and keep parallel resonance status under a wide range of loads. Experiments conducted under actual operating conditions verify the feasibility of the proposed scheme under the modal resistance range from 7.40 to 500 Ω and the vibration range from 20% to 100%. Moreover, with the aid of a laser displacement sensor, our scheme is verified to have a vibration amplitude control accuracy better than 2% over a tenfold load variation. This research could be helpful for the driving and control of HPPSs operating in a wide range.

Keywords: high-power piezoelectric systems; parallel resonance tracking; vibration amplitude control; transformer ratio arm bridge; pulse-based phase detector

1. Introduction

High-power piezoelectric systems (HPPSs) are used in a large range of applications, such as ultrasonic welding, cutting and actuators [1–4]. In high-power situations, it is crucial to effectively convert the electrical energy into the mechanical vibration in the piezoelectric transducers (PTs) [5–8]. Generally, researchers excite PTs at their mechanical resonance frequency, that is, the series resonance frequency (f_s), where the minimum excitation voltage is required [1,9]. However, as the vibration amplitude increases, an additional loss near f_s degrades the performance of the PTs in high power [10,11]. It is attributed to the dielectric loss which is related to the input current in HPPSs [12]. Therefore, exciting the PTs at the parallel resonance frequency (f_p) with the minimum excitation current can achieve the optimal efficiency. For the HPPSs operating under high vibration amplitude, high excitation voltage is required at f_p [12]. However, different materials and processes result in wide range of loads in some ultrasonic machining, such as welding and cutting [13,14]. The load increases the required excitation voltage, leading to the risk of electrical breakdown. Therefore, avoiding the excessive rise up of excitation voltage under high load conditions becomes a challenge for HPPSs. Meanwhile, the wide range of loads has a significant impact on the impedance characteristics, leading to another challenge in providing sufficient drive capability over the operating range.

In most ultrasonic systems, piezoelectric transducers (PTs) need to be excited in the resonant mode [1,9]. Besides, different vibration amplitudes are required for different processing materials [14,15].

For the PT working at light loading conditions, the excitation voltage and current are almost in phase at f_s and f_p, while the impedance reaches the minimum and maximum near f_s and f_p, respectively [16]. Therefore, the working frequency can be tracked by a phase locking loop (PLL) or impedance extremum search [17]. Meanwhile, the vibration amplitude can be controlled through current and voltage driving modes at f_s and f_p, respectively [9,16]. However, as the load increases, two pairs of zero phase frequencies and the impedance extreme frequencies gradually deviate from f_s and f_p [17]. In order to enlarge the operating load range, schemes based on the impedance or admittance calculation are proposed, such as the maximum target impedance scheme and the admittance circle tracking scheme [1,18]. However, these schemes require complicated software operations to calculate the frequency deviation and the vibration amplitude. With the aid of a transformer ratio arm bridge (TRAB), a vibration amplitude signal is obtained online in an ultrasonic motor control scheme under different operating conditions [19]. Moreover, this signal is in phase with the excitation current at f_p, so the parallel resonance detection can be achieved by detecting the phase between the vibration and the excitation current signals. However, the excitation current can be extremely discontinuous and harmonic-rich in the HPPSs over a wide operating range, leading to a new challenge for phase detection.

In order to drive the HPPSs at load optimization frequency under a wide range of loads with controllable vibration amplitudes, a driving and control scheme is proposed in this paper. We first analyze the impact of different loads on the impedance characteristics, and propose the load optimization frequency tracking mode. Second, in order to provide the sufficient drive capability, the effect of the inverter combined with an LC matching circuit is analyzed under different operating conditions. Then, the pulse-based phase detector (PBPD) is proposed to overcome the challenge of phase detection over a wide operating range. Finally, the proposed scheme is verified under actual operating conditions in terms of the frequency tracking and vibration control.

2. Electrical Architecture

2.1. Equivalent Models

An HPPS can be characterized by electromechanical models (A and B) deduced from an electrical model, as shown in Figure 1 [12].
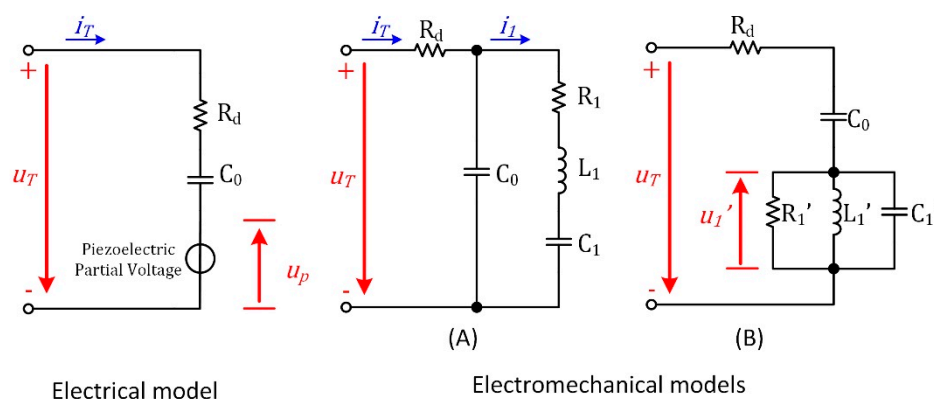
Figure 1. Electrical and Electromechanical models of high-power piezoelectric systems (HPPSs).

In the electromechanical models, the dielectric property is characterized by C_0 and R_d. For model A, which is similar to the classic Butterworth-Van Dyke (BVD) model [20,21], the series R_1, L_1 and C_1 characterize the modal damping, mass and stiffness, respectively. Under the steady state of sinusoidal

excitation, the model A can be converted to the model B [19]. In this model, the parameters can be calculated by

$$\begin{cases} R'_1 = \frac{1}{B_0^2 R_1} \\ L'_1 = \frac{C_p}{B_0^2} \\ C'_1 = B_0^2 L_1 \end{cases},$$

(1)

where

$$\begin{cases} B_0 = \omega C_0 \\ C_p = \frac{C_0 C_1}{C_0 + C_1} \end{cases}.$$

(2)

In this paper, some electrical characteristics under sinusoidal excitation can be expressed in complex vectors form written in bold letters, such as

$$\begin{cases} \boldsymbol{U'_1} = U'_1 e^{j\omega t} \\ \boldsymbol{U_T} = U_T e^{j\omega t} \\ \boldsymbol{I_T} = I_T e^{j\omega t} \end{cases},$$

(3)

where $\boldsymbol{U'_1}$ is the partial voltage of the parallel RLC part, and $\boldsymbol{U_T}$ and $\boldsymbol{I_T}$ are the excitation voltage and current of the transducer, respectively. Here, $\boldsymbol{Z'_1} = \boldsymbol{U'_1}/\boldsymbol{I_T}$ is defined as the impedance of the parallel RLC part, which satisfies the relationship

$$\boldsymbol{Z'_1} = 1 / \left(\frac{1}{R'_1} + j\omega L'_1 + \frac{1}{j\omega C'_1} \right).$$

(4)

Then, we define θ to be the phase angle of $\boldsymbol{Z'_1}$, that is, the phase between $\boldsymbol{U'_1}$ and $\boldsymbol{I_T}$. Therefore, it can be inferred that $\theta = 0$ at f_p without the influence of R_1, because the parallel RLC part resonates at f_p according to

$$f_p = \frac{1}{2\pi \sqrt{L'_1 C'_1}}.$$

(5)

Moreover, when comparing with the electrical model, it can be noted that the partial voltage u'_1 in the model B corresponds to the piezoelectric voltage u_p in the electrical model, which is proportional to the vibration amplitude [12]. Therefore, u'_1 can be used for vibration and parallel resonance detection without additional calculation.

In this paper, we use a DUKANE 20 kHz 3300 W piezoelectric transducer, a 1:1.5 transducer amplitude transformer, and a φ70 mm plastic welding horn to construct a typical HPPS used for ultrasonic welding. The parameters of the HPPS are shown in Table 1. It should be noted that, in actual operating conditions, R_1 increases from 7.40 Ω under no load condition to 200~500 Ω under high load conditions.

Table 1. Parameters of the BVD model for the HPPS.

Parameters	R_d (Ω)	C_0 (nF)	C_1 (nF)	L_1 (mH)	R_1 (Ω)
value	7.26	18.93	0.1696	370.4	7.40~500

2.2. Impedance Characteristics Analysis

To analyze the influence of wide range of loads in an HPPS, the variations in U_T and I_T are calculated under a constant vibration. First, we set U'_1 to be a typical value 1700 V, and I_T can be calculated as

$$I_T = \left| \frac{U'_1}{\boldsymbol{Z'_1}} \right|.$$

(6)

Then, U_T is deduced to be

$$U_T = \left| I_T \left(\mathbf{Z}'_1 + R_d + 1/j\omega C_0 \right) \right|. \tag{7}$$

Therefore, the variations in U_T and I_T under different excitation frequencies are calculated and demonstrated in Figure 2a,b, respectively, in which R_1 is taken as four different typical values of 7.4, 50, 100 and 200 Ω. This analysis shows that I_T increases linearly while U_T increases slightly at f_p as R_1 increases. Therefore, it can be inferred that the wide range of loads leads to an equal variation range of I_T at f_p. Furthermore, the current variation range is further expanded to over a hundred times when the vibration amplitude is controlled from 20% to 100% in our system.

| (a) | (b) |
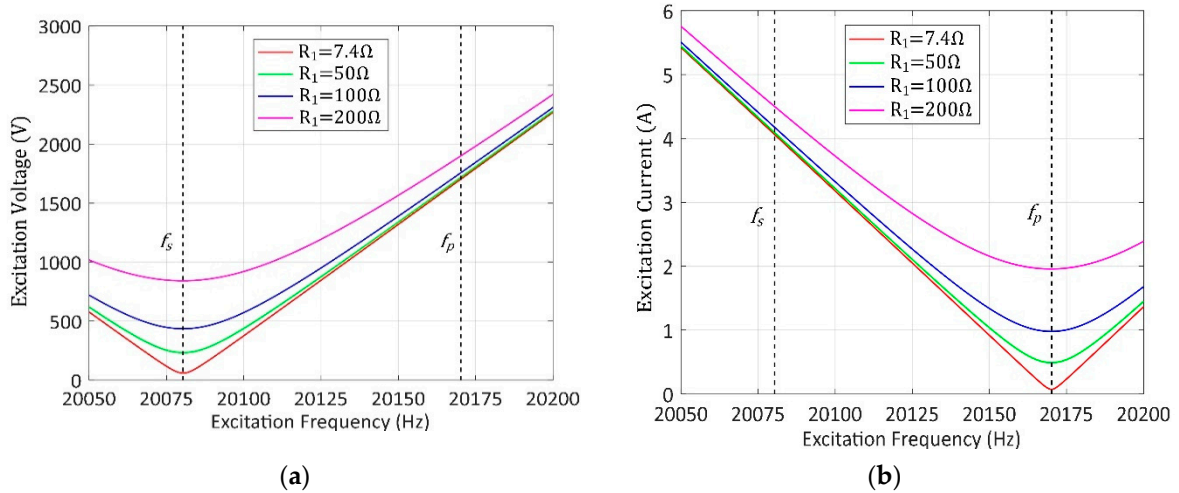
Figure 2. Variations in excitation voltage (**a**) and current (**b**) under the same vibration amplitude.

Moreover, we analyze the influence of R_d from the perspective of the dielectric voltage drop rate calculated as $I_T R_d / U_T$, as shown in Figure 3. It shows that R_d has the greatest impact at f_s, especially under light load conditions. However, the dielectric voltage drop rate decreases to less than 1% near f_p. Therefore, the influence of R_d on the impedance characteristics can be ignored in our scheme.
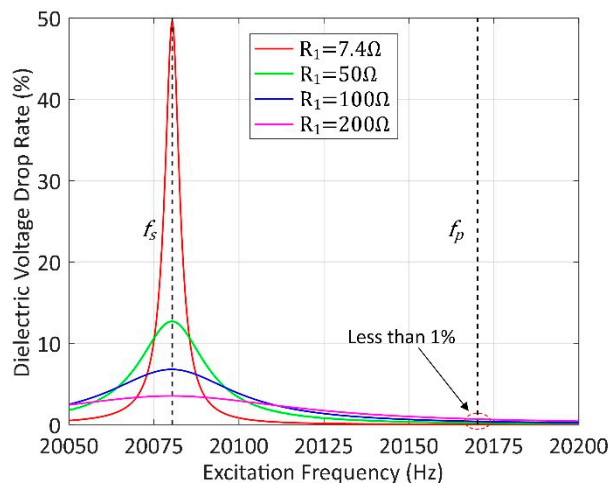
Figure 3. Dielectric voltage drop rate under different frequencies and loads.

Further, we analyze the variations of U_T and I_T near f_p from the perspective of the phase θ under the constant vibration amplitude (U_1' equals to 1700 V), as shown in Figure 4a,b, respectively. The relationships of U_T and I_T are deduced as

$$I_T = \frac{U_1'}{R_1' \cos\theta}, \tag{8}$$

$$U_T = \left| U_1' + I_T(R_d + 1/j\omega C_0) \right|. \tag{9}$$
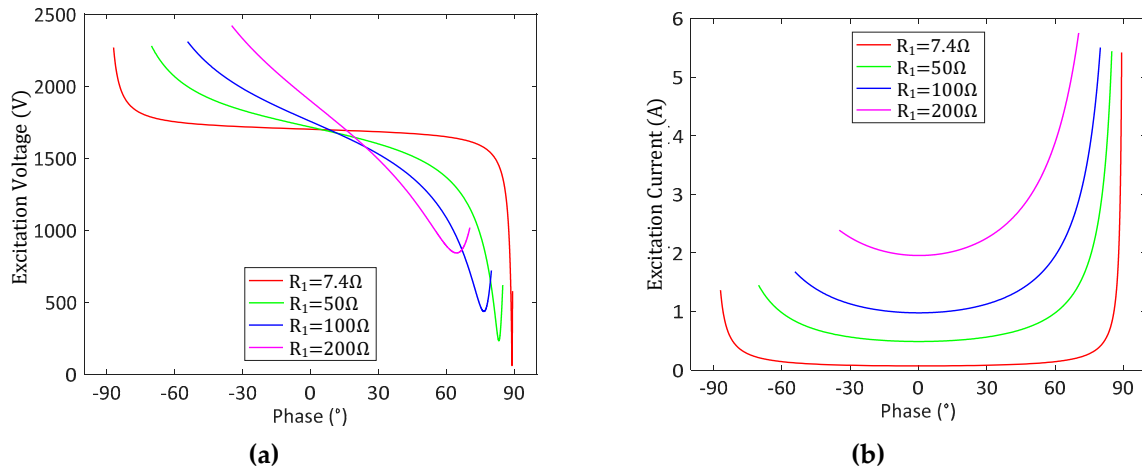
Figure 4. Variations in excitation voltage (**a**) and current (**b**) under different phase θ.

The curves of U_T shows that U_T increases with R_1 at f_p, and decreases with a slope positively related to R_1 as θ increases. Meanwhile, it shows that I_T is very close to the minimum near the zero phase due to the inverse relationship with $\cos\theta$. The analysis above suggests that slight phase difference has little influence on the impedance characteristics. Especially, an appropriate phase difference, such as 20°, can prevent the rise of U_T under high load conditions with a negligible rise of I_T. Therefore, we suggest the load optimization frequency to be slightly lower than f_p with θ near 20° in our typical HPPS.

3. Proposed Driving Scheme

3.1. Electrical Architecture

The proposed scheme contains a rectifier bridge, a full-bridge inverter, an LC matching circuit and a transformer, as shown in Figure 5.
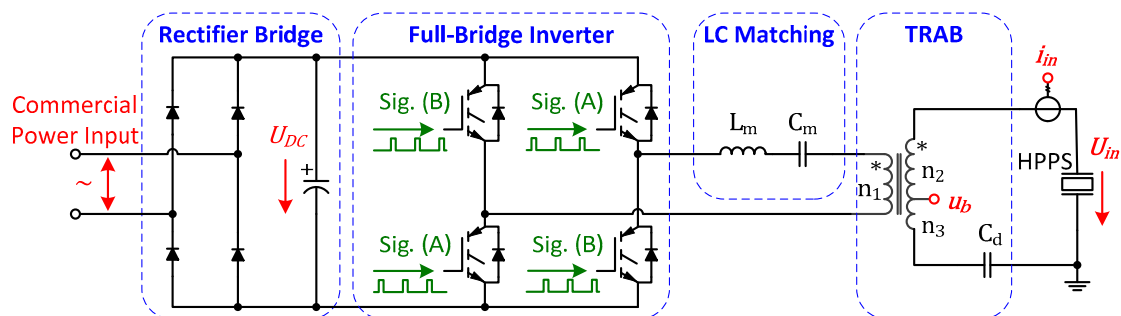
Figure 5. Electrical architecture of the proposed scheme.

The commercial power (220 V 50 Hz) is rectified into the DC power U_{DC}, and then inverted to the AC power in ultrasonic frequency. A series LC matching circuit is used for DC isolating and harmonic filtering. More importantly, the specific configuration of L_m and C_m is also related to impedance matching and vibration excitation, which are analyzed in the next sector. Since a transformer ratio arm bridge (TRAB) is easy to be intergraded with little impact on the electrical circuit [16], it is adopted to detect the partial voltage u_1' online. A tap is drawn from the secondary side of the transformer with the coil turns satisfying $n_2 \gg n_3$, and a detection capacitor C_d is connected into the circuit, which satisfies

$$C_d = \frac{n_2 + n_3}{n_3} C_0. \tag{10}$$

Therefore, the bridge voltage, that is, the transformer tap voltage u_b satisfies the relationship

$$\boldsymbol{U_b} = \frac{n_3}{n_2 + n_3} \boldsymbol{U_T} - j\omega C_d \boldsymbol{I_T} = \frac{n_3}{n_2 + n_3} \boldsymbol{U_1'}. \tag{11}$$

In the proposed scheme, we configure $n_1 = 22$, $n_2 = 155$, $n_3 = 4$ and $C_d = 752$ nF according to the analysis above.

3.2. Electrical Properties

Under the driving of the gate signals, the inverter continuously changes the switching state, as shown in Figure 6. The input current to the HPPS i_{in} rises up in the conduction zones and falls down in the freewheeling zones, then i_{in} becomes zero and the inverter enters high resistance zones. As the duty cycle d of the gate signals increases, the conduction zones become wider, leading to the increase in the vibration amplitude. However, the situation is much different under different d.
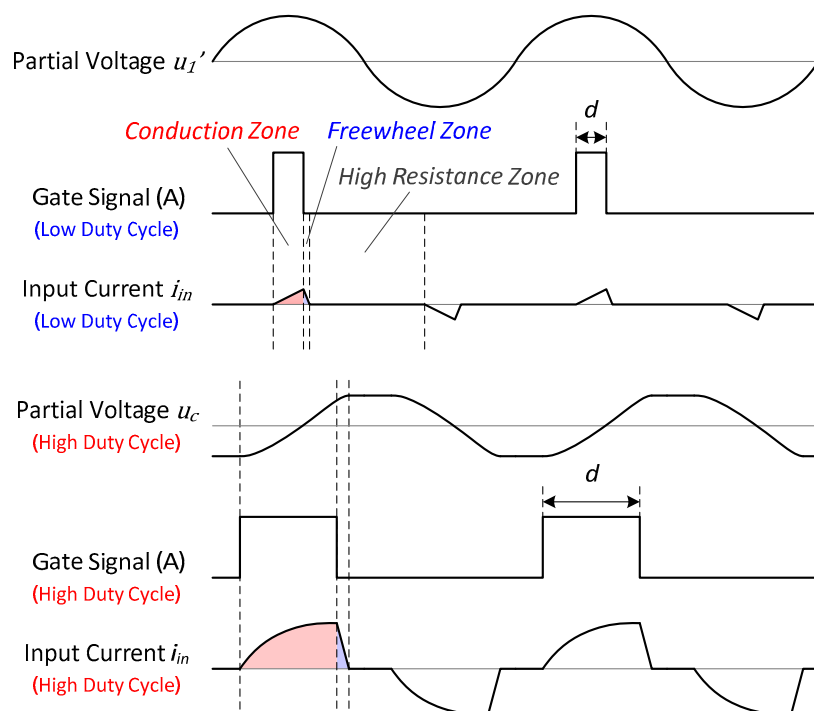
Figure 6. Typical waveforms of the proposed scheme.

In order to analyze the electrical properties under the steady state near f_p, the electric architecture is simplified by equivalent transformation, as shown in Figure 7, leading to

$$\begin{cases} L'_m = k^2 L_m \\ C'_m = \frac{1}{k^2} C_m \\ U'_{DC} = kU_{DC} \end{cases}, \tag{12}$$

where k is the transformer ratio. L'_m, C'_m and U'_{DC} are the matching inductance, matching capacitance and DC voltage after transformation, respectively. We also define u_C as the sum voltage of C'_m and C_0.
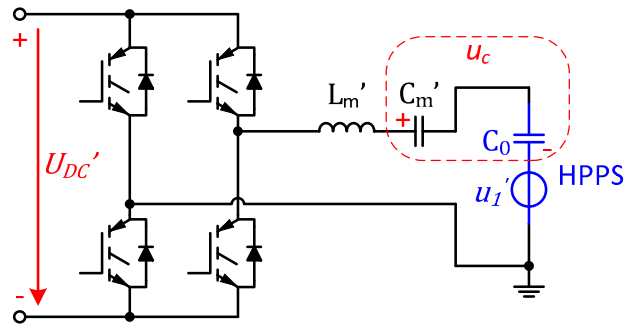
Figure 7. Equivalent electrical circuit of the proposed scheme.

First, we analyze the situations with low duty cycle d. Under these conditions, i_{in} is always small, leading to negligible u_C. Therefore, in the conduction zones, there exists

$$\frac{di_{in}}{dt} = \frac{1}{L'_m}\left(U'_{DC} - u'_1\right), \tag{13}$$

while there exists

$$\frac{di_{in}}{dt} = \frac{1}{L'_m}\left(-U'_{DC} - u'_1\right) \tag{14}$$

in the freewheel zones. i_{in} and other related waveforms are shown in Figure 6. Since only the fundamental wave can excite the modal vibration, we use the Fourier series to extract it in i_{in} to consider as the excitation current i_T of the HPPS, which can be calculated as

$$i_T = \frac{\omega_p}{\pi}\int_{-\frac{\pi}{\omega_p}}^{\frac{\pi}{\omega_p}} i_{in}\cos\left(\omega_p t\right)dt\cos\left(\omega_p t\right) + \frac{\omega_p}{\pi}\int_{-\frac{\pi}{\omega_p}}^{\frac{\pi}{\omega_p}} i_{in}\sin\left(\omega_p t\right)dt\sin\left(\omega_p t\right). \tag{15}$$

When we define u'_1 to be in phase with $\sin\left(\omega_p t\right)$, and i_{in} should also be in phase. Therefore, the first term in Equation (15) equals to zero. On the other hand, the conduction and freewheeling zones are concentrated near the peak of $\sin\left(\omega_p t\right)$. Therefore, Equation (15) can be approximated as

$$i_T = \frac{\omega_p}{\pi}\int_{-\frac{\pi}{\omega_p}}^{\frac{\pi}{\omega_p}} |i_{in}|dt\sin\left(\omega_p t\right), \tag{16}$$

By consideration of Equations (13), (14) and (16), it can be deduced that

$$i_T = 4(A + B)\sin\left(\omega_p t\right), \tag{17}$$

where A and B correspond to the effects of the conduction zones and the freewheeling zones, respectively, deduced as

$$\begin{cases} A = \frac{d^2}{2L'_m f_p}\left(U'_{DC} - U'_1\right) \\ B = \frac{d^2}{2L'_m f_p}\frac{U'_{DC} - U'_1}{U'_{DC} + U'_1}\left(U'_{DC} - U'_1\right) \end{cases}. \tag{18}$$

According to $U'_1 = I_T R'_1$ at f_p, the relationship between U'_1 and d can be derived as

$$U'_1 = \frac{-(1 + 2D) + \sqrt{1 + 12D + 4D^2}}{2}U'_{DC}, \tag{19}$$

where

$$D = \frac{d^2 R'_1}{2L'_m f_p}. \tag{20}$$

Therefore, L_m is inversely proportional to U'_1 under the same load and duty cycle.

For the conditions where the inverter is driven with high duty cycle d, the capacitor voltage u_C is considerable, leading to Equations (21) and (22) in the conduction zones and freewheel zones, respectively. This mechanism leads to the heaping of the current waveform, as shown in Figure 6, which greatly increases the excitation current to the HPPS. Although it is difficult to analyze the current waveform further, the behavior of the inverter can be analyzed from the perspective of the input voltage u_{in} under these situations. The conduction zones gradually dominate in the waveform of u_{in}, approaching to a bidirectional pulse wave with increasing d, as shown in Figure 8.

$$\frac{di_{in}}{dt} = \frac{1}{L_m}\left(U'_{DC} - u_C - u'_1\right). \tag{21}$$

$$\frac{di_{in}}{dt} = \frac{1}{L_m}\left(-U'_{DC} - u_C - u'_1\right). \tag{22}$$
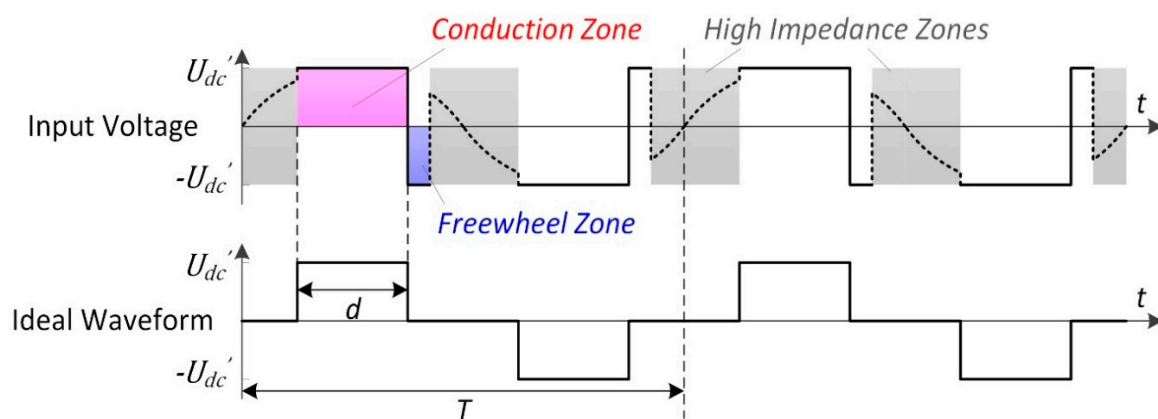
Figure 8. Waveforms of the input voltage and the corresponding bidirectional pulse under high duty cycle.

Here, it is important to configure LC matching circuit to offset the capacitive reactance of C_0 and make the circuit purely resistive at f_p, satisfying

$$2\pi f_p L_m - \frac{1}{2\pi f_p C_m} = k^2\frac{1}{2\pi f_p C_0}. \tag{23}$$

Therefore, it can be noted that the partial voltage u_1' is equal to fundamental wave of the output voltage of the inverter under the matching condition above, satisfying

$$U_1' = \frac{4U_{DC}'}{\pi} \sin \pi d. \tag{24}$$

This relationship suggests that the scheme can excite U_1' to the maximum value of $\frac{4}{\pi}kU_{DC}$ without being affected by the load.

Due to the analyzed above, we configure $L_m = 143$ µH and $C_m = 870$ nF. Here, we use MATLAB/Simulink (MathWorks, Natick, MA, USA, 2017b) to simulate the relationship among d, R_1 and U_1', as shown in Figure 9. It shows that U_1' increases smoothly with d under different loads. This result verifies the drive capability of our scheme under a wide range of loads with adjustable vibration amplitude.
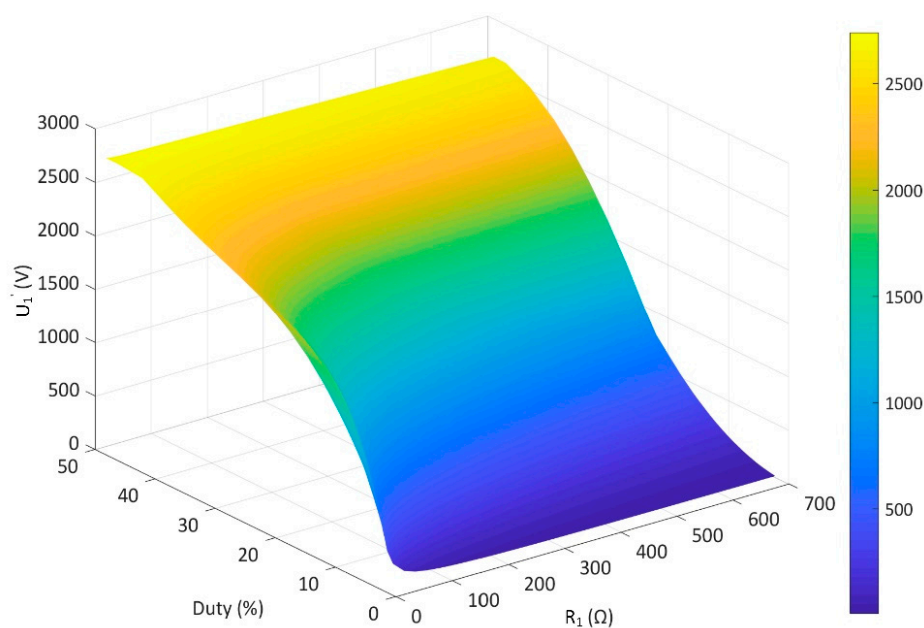
Figure 9. Simulation result of vibration amplitude under different loads and duty cycle.

4. Detection and Control

4.1. Pulse Based Phase Detector

In order to maintain constant vibration amplitude and keep operating near f_p, the amplitude of u_1' and its phase θ with I_{in} need to be detected. Owing to the TRAB integrated in our scheme, u_1' is extracted via the signal u_b, which is strong and pure under most conditions. Therefore, it can be reliably digitized through the zero-crossing comparator after squelch. Meanwhile, I_{in} is detected by a feed-through current transformer. However, filtering and digitizing i_{in} is difficult due to the discontinuous and harmonic-rich in the large variation range.

In this scheme, a pulse-based phase detector (PBPD) is proposed. Since the input current i_{in} almost occurs in the conduction zones, a PWM gate signal is used instead of the i_{in}. A classical digital phase detector based on D flip-flops is adopted to generate a phase detection signal. The timing diagram of the relevant signals and the phase detector circuit are shown in Figures 10 and 11, respectively.
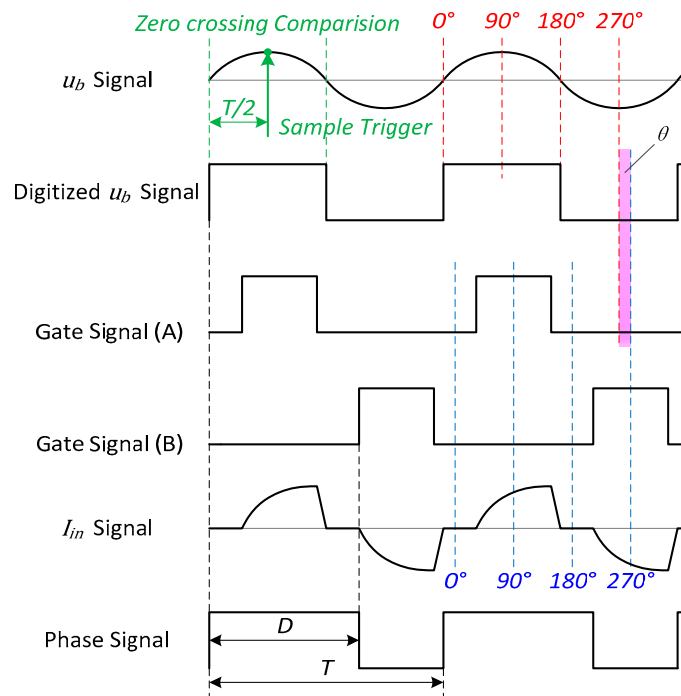
Figure 10. Timing diagram of the relevant signals of pulse-based phase detector (PBPD).
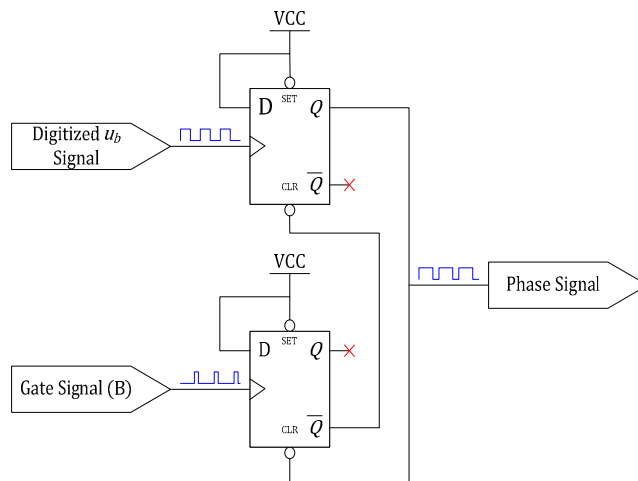
Figure 11. Structure of the D flip-flops-based detector.

In the proposed scheme, we use the gate signal B but not A to avoid the potential competitive risk, and define the pulse center to be 270°. Therefore, the phase θ can be calculated though the relationship

$$\theta = 360° * \frac{D + d/2}{T} - 270°, \tag{25}$$

where D and T are the pulse width and the cycle of the phase signal, respectively. Affected by the variation in the current waveform under different conditions, the phase θ obtained by PBPD has a small deviation, which will be further analyzed in the experiment.

This signal is also used in the detection of U_b, which triggers a $T/4$ peak sampling timer on the rising edge, as shown in Figure 10.

4.2. Control Realization

Due to the perturbation of U_{DC} and variation of load, a vibration close loop is needed in the proposed scheme. As d is deduced to be in positive correlation to U'_1, the control logic is established as

$$\Delta d = K_{p,d}\left(U_{b,target} - U_b\right), \tag{26}$$

where U_b is the feedback parameter, $U_{b,target}$ is the vibration target voltage, and $K_{p,d}$ is the proportional control parameter in the vibration amplitude controller.

Moreover, due to the change of temperature and the coupling stiffness caused by the loads, a frequency closed loop needs to be executed in parallel with the vibration close loop. Since θ is inversely related to frequency and equal to zero at f_p , the control logic is established as

$$\Delta f = K_{p,f}\theta, \tag{27}$$

where $K_{p,f}$ is the proportional control parameter in the frequency controller.

5. Experimental Results

5.1. Frequency Tracking Verification

The experimental setup is demonstrated in Figure 12. Here, the HPPS is fixed on a pneumatic thruster and pressed against a damp cloth. We apply different loads to the HPPS by adjusting the cylinder pressure of the thruster. Meanwhile, the waveforms of U_{in}, I_{in}, U_b and the gate signal A are measured by a Tektronix TDS 2024B oscilloscope, and the waveforms of four extreme operating conditions are shown in Figure 13. Here, 100% controlled vibration amplitude corresponds to about 1700 V of U'_1. The sampling period of the oscilloscope is 0.04 μs in the experiments, and the accuracy is 0.04 per division for each channel. This result shows that the center of the pulse coincides with the peak of u_b, indicating that the frequency tracking meets the design. Meanwhile, the current waveforms are basically consistent with the analysis. The difference is caused by a weak leaking current in the high-resistance region, which may be attributed to the influence of the parasitic capacitance of the IGBT modules in the inverter.
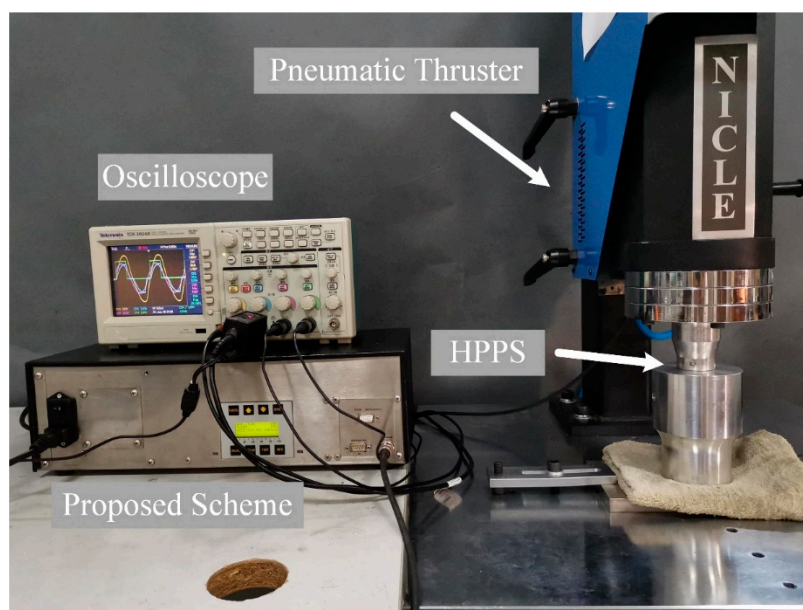
Figure 12. Experimental setup of frequency tracking verification.
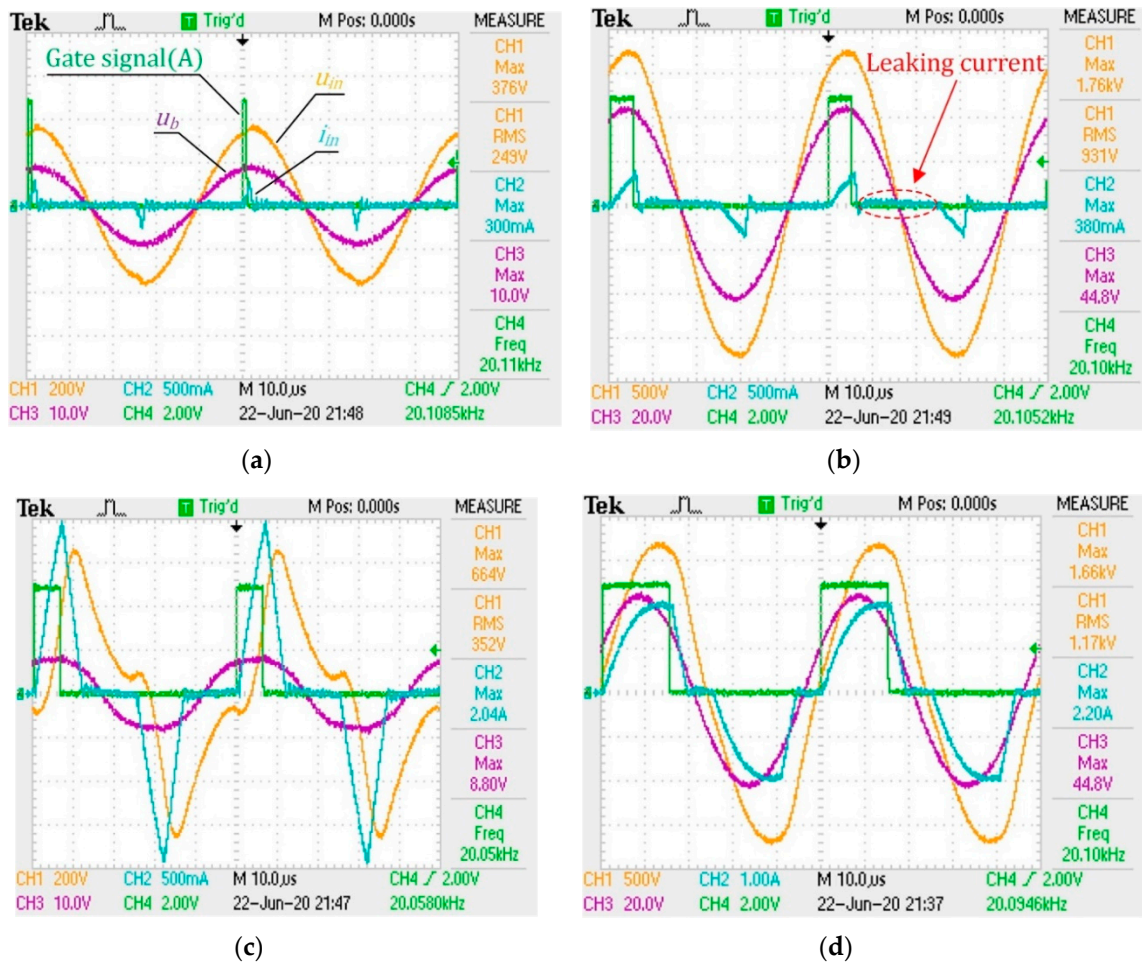
Figure 13. Waveforms of extreme operating conditions: (**a**) R_1 equals 7.40 Ω under 20% vibration amplitude; (**b**) R_1 equals 7.40 Ω under 100% vibration amplitude; (**c**) R_1 equals 500 Ω under 20% vibration amplitude; (**d**) R_1 equals 200 Ω under 100% vibration amplitude.

Further, we perform Fourier transform to extract the fundamental wave of I_{in}, and the actual θ is calculated and demonstrated in Figure 14. This result shows that the phase difference is about 15°~25° under most operating conditions but relatively large under no load conditions (R_1 equals to 7.40 Ω). It is inferred that the load optimization frequency is slightly lower than f_p, with θ near 20° in Section 2.2. The experiment result verifies this inference in which the actual excitation peak voltage is 1.76, 1.58, 1.58 and 1.62 kV when R_1 equals to 7.40, 50, 100 and 200 Ω, respectively.

5.2. Vibration Control Verification

In this experiment, the vibration is tracked in different amplitudes by the proposed scheme and the actual vibration amplitude is measured by a KEYENCE LK-H008 laser displacement sensor. The measurement setup is shown in Figure 15. Each measurement is repeated five times, as shown in Figure 16. The result shows the linear relationship between our controlled vibration amplitude and the actual vibration amplitude. It verifies the reliability of our scheme in vibration control, which can be suitable for different processes.
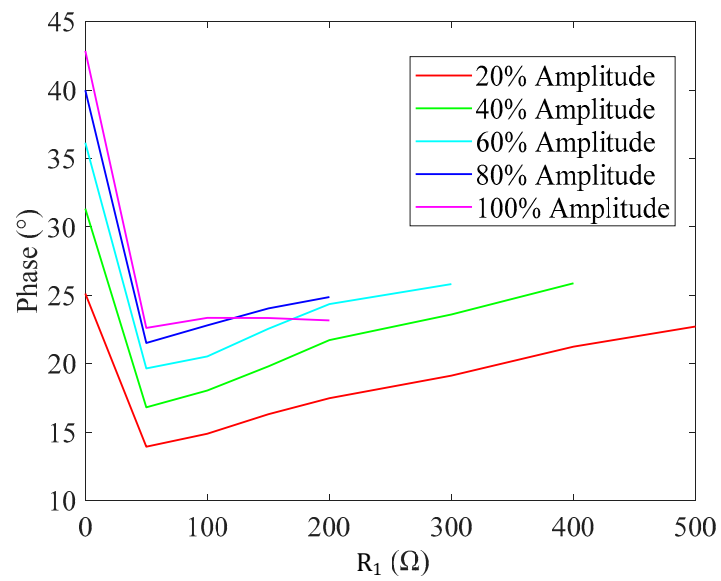
Figure 14. Phase deviation under different loads and vibration amplitudes.

Figure 15. Experimental setup of vibration control verification.
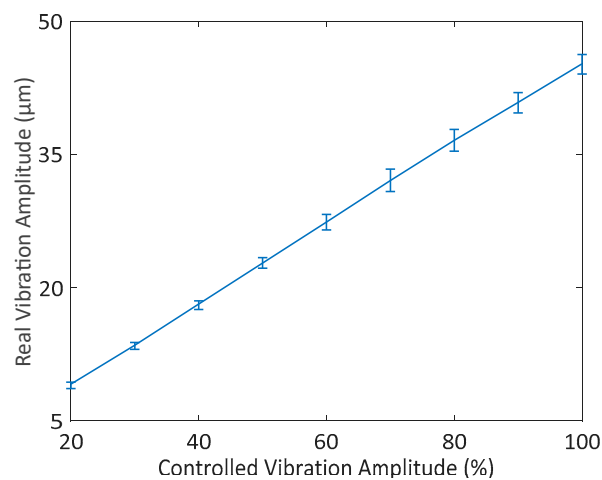
Figure 16. Real vibration amplitude under different control targets.

5.3. Vibration Stability under Variable Load

In order to verify the stability of vibration control in varying load condition, we set target vibration amplitude to 30%, and increase the load gradually using water. Meanwhile, the laser senor measures the actual vibration amplitude. The proposed scheme also calculates and records R_1 in real time according to the equation:

$$R_1 = \frac{I_T \cos\theta}{U_1'(\omega C_0)^2}. \tag{28}$$

The variations in the actual vibration amplitude and R_1 are shown in Figure 17. It shows that R_1 gradually increases 10 times after startup, while the fluctuation in the actual vibration amplitude is within 2%. This result verifies the feasibility in a wide range of loads. On the other hand, it also demonstrates the dynamic adaptability of our scheme. Although the capability of frequency tracking and vibration control is verified, the HPPSs under transient state have more complex characteristics, which should be further considered in the dynamic process.
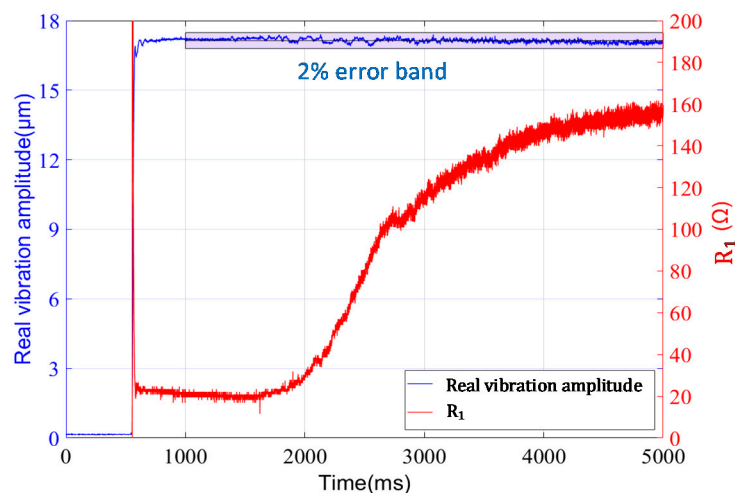
Figure 17. Variation in vibration amplitude under varying load.

6. Conclusions

This paper demonstrates that the proposed scheme is capable of frequency tracking and vibration control under a wide operating range. First, the impedance analysis indicates that the excitation current I_T varies in a wide range under different loads near f_p. The analysis also indicates that a slight

deviation in phase θ affects the impedance characteristics little. Especially, we suggest that the load optimization frequency with about 20° phase difference can help avoid the excessive rise up of the excitation voltage under high load conditions. Second, the electrical architecture is built, and the drive capability of the scheme is verified in wide range of loads and different vibration amplitudes. Then, the pulse-based phase detector (PBPD) is proposed, which can get the phase signal over a wide operating range with acceptable precision. The experiments verify the feasibility of PBPD and vibration amplitude control under the resistance range from 7.40 to 500 Ω and the vibration range from 20% to 100%. Finally, the experiment verifies that the accuracy of the vibration control is within 2% via a laser displacement sensor under varying load. The proposed scheme could be very useful for the HPPSs working in complex conditions, like ultrasonic welding and cutting.

Author Contributions: Conceptualization and methodology, T.Y. and M.Y.; Software, T.Y. and Z.F.; validation, Y.Z. and H.W.; writing—original draft preparation, T.Y. and Y.Z.; visualization, Y.Z. and Z.F.; supervision, M.Y. and W.J. All authors have read and agreed to the published version of the manuscript.

Conflicts of Interest: The authors declare no conflict of interest.

References

1. Wang, J.D.; Jiang, J.J.; Duan, F.J.; Zhang, F.M.; Liu, W.; Qu, X.H. A Novel Fast Resonance Frequency Tracking Method Based on the Admittance Circle for Ultrasonic Transducers. *IEEE Trans. Ind. Electron.* **2020**, *67*, 6864–6873. [CrossRef]
2. Rani, M.R.; Prakasan, K.; Rudramoorthy, R. Studies on Thermo-Elastic Heating of Horns used in Ultrasonic Plastic Welding. *Ultrasonics* **2015**, *55*, 123–132. [CrossRef] [PubMed]
3. Jiang, X.; Zhang, X.; Zhu, X.; Sui, H.; Zhang, D. Study of Phase Shift Control in High-Speed Ultrasonic Vibration Cutting. *IEEE Trans. Ind. Electron.* **2018**, *65*, 2467–2474. [CrossRef]
4. An, D.; Yang, M.; Zhuang, X.; Yang, T.; Meng, F.; Dong, Z. Dual Traveling Wave Rotary Ultrasonic Motor with Single Active Vibrator. *Appl. Phys. Lett.* **2017**, *110*, 143507. [CrossRef]
5. Ghenna, S.; Giraud, F.; Giraud-Audine, C.; Amberg, M. Vector Control of Piezoelectric Transducers and Ultrasonic Actuators. *IEEE Trans. Ind. Electron.* **2018**, *65*, 4880–4888. [CrossRef]
6. Nazemi, H.; Balasingam, J.A.; Swaminathan, S.; Ambrose, K.; Nathani, M.U.; Ahmadi, T.; Lopez, Y.B.; Emadi, A. Mass Sensors Based on Capacitive and Piezoelectric Micromachined Ultrasonic Transducers-CMUT and PMUT. *Sensors* **2020**, *20*, 2010. [CrossRef] [PubMed]
7. Fiorillo, A.S.; Pullano, S.A.; Bianco, M.G.; Critello, C.D. Ultrasonic Transducers Shaped in Archimedean and Fibonacci Spiral: A Comparison. *Sensors* **2020**, *20*, 2800. [CrossRef] [PubMed]
8. Nguyen, T.H.L.; Park, S. Multi-Angle Liquid Flow Measurement Using Ultrasonic Linear Array Transducer. *Sensors* **2020**, *20*, 388. [CrossRef] [PubMed]
9. Liu, X.; Colli-Menchi, A.I.; Gilbert, J.; Friedrichs, D.A.; Malang, K.; Sánchez-Sinencio, E. An Automatic Resonance Tracking Scheme With Maximum Power Transfer for Piezoelectric Transducers. *IEEE Trans. Ind. Electron.* **2015**, *62*, 7136–7145. [CrossRef]
10. Umeda, M.; Nakamura, K.; Ueha, S. The Measurement of High-Power Characteristics for a Piezoelectric Transducer Based on the Electrical Transient Response. *Jpn. J. Appl. Phys.* **1998**, *37*, 5322–5325. [CrossRef]
11. Uchino, K.; Zheng, J.H.; Chen, Y.H.; Du, X.H.; Ryu, J.; Gao, Y.; Ural, S.; Priya, S.; Hirose, S. Loss mechanisms and high power piezoelectrics. *J. Mater. Sci.* **2006**, *41*, 217–228. [CrossRef]
12. Yang, T.; Zhu, Y.; Li, S.; An, D.; Yang, M.; Cao, W. Dielectric loss and thermal effect in high power piezoelectric systems. *Sens. Actuators A Phys.* **2019**, *303*, 111724. [CrossRef]
13. Wu, H.; Yang, M.; Yang, T.; An, D. Development of web-based communication for ultrasonic power supply. In Proceeding of the 2nd International Conference on Communication and Information, Wuhan, China, 7–9 November 2017.
14. Zang, Y.D. *Sandwich Piezoelectric Transducers and Their Applications*, Chinese ed.; Science Press: Beijing, China, 2006.

15. Zhu, Y.; Yang, T.; Fang, Z.; Shiyang, L.; Cunyue, L.; Yang, M. Contact modeling for control design of traveling wave ultrasonic motors. *Sens. Actuators A Phys.* **2020**, *310*, 112037. [CrossRef]

16. Zhang, H.; Wang, F.; Zhang, D.; Wang, L.; Hou, Y.; Xi, T. A new automatic resonance frequency tracking method for piezoelectric ultrasonic transducers used in thermosonic wire bonding. *Sens. Actuator A-Phys.* **2015**, *235*, 140–150. [CrossRef]

17. Zhao, C.S. *Ultrasonic Motors Technologies and Application*, Chinese ed.; Science Press: Beijing, China, 2007.

18. Di, S.; Fan, W.; Li, H. Parallel resonant frequency tracking based on the static capacitance online measuring for a piezoelectric transducer. *Sens. Actuator A-Phys.* **2018**, *270*, 18–24. [CrossRef]

19. Fang, Z.; Yang, T.; Zhu, Y.; Li, S.; Yang, M. Velocity Control of Traveling-Wave Ultrasonic Motors Based on Stator Vibration Amplitude. *Sensors* **2019**, *19*, 5326. [CrossRef] [PubMed]

20. Butterworth, S. On Electrically-maintained Vibrations. *Proc. Phys. Soc. Lond.* **1914**, *27*, 410–424. [CrossRef]

21. Dyke, K.S.V. The Piezo-Electric Resonator and Its Equivalent Network. *Proc. Inst. Radio Eng.* **1928**, *16*, 742–764.